# Reinforcement mechanisms of low-strength fragile material under in-plane shear loading by composite lattice structures

Peixin Yang [a,b], Wu Yuan [a,b,*], Hongwei Song [a,b], Chenguang Huang [b]

[a] *Key Laboratory for Mechanics in Fluid-Solid Coupling Systems, Institute of Mechanics, Chinese Academy of Sciences, Beijing 100190, China*
[b] *School of Engineering Sciences, University of Chinese Academy of Sciences, Beijing 100049, China*

## ARTICLE INFO

## ABSTRACT

Ablative materials are always seriously damaged under the shear force induced by the hypersonic airflow when used in thermal protection systems. An effective method to improve the shear strength of the low-strength fragile material by composite lattice structures, has been presented in the present study. The reinforcement mechanisms of the lattice structures were then revealed both experimentally and theoretically. The experimental results showed that there exists an interaction effect between the fragile material and the lattice. The integrated shear strength was obviously higher than the sum of the fragile material and the lattice. A theoretical model was also developed to investigate the interaction effect. It was found that the interfacial bonding between the lattice and the matrix plays a significant role in reinforcement mechanism. Finally, the effect of geometrical parameters (such as topological configurations, relative densities, and cell size) on the shear strength of the fragile material, is thoroughly discussed.

## 1. Introduction

The heat-resistant bottom of the return capsule encounters extreme conditions during reentry. The designers of this capsule require a structure that can meet the requirements of light weight, reliability, reusability and high load-bearing performance [1–4]. There are nowadays honeycomb reinforced ablative heat-resistant bottoms, and fiber woven pre-fabricated body-impregnated ablative heat-resistant bottom designs, that have successfully achieved re-entry [5,6]. Honeycomb reinforced ablative heat-resistant bottom is a two-dimensional ordered honeycomb structure that functions as the reinforcing phase of the ablative material. There are two main problems for the foam reinforced types thermal protection systems. At first, the shear resistance of the two-dimensional honeycomb structures is relatively weak, so it is prone to an aerodynamic spalling behaviour [7]. Secondly, the preparation process is complicated. The foreign single-hole infusion technology takes five months to form, while the Chinese vacuum-integrated infusion technology has high requirements for the ablative material [8].

Lattice is a light-weight multifunctional material with excellent properties, such as high porosity, ultra-light weight, highly specific stiffness and specific strength, and high-energy absorption [9–12]. Moreover, the lattice, as the tensile-dominated structure, has a higher

shear strength than a bending-dominated structure (such as the honeycomb) [9]. Lattice spaces filled with ablative materials may have more advantages than honeycomb spaces filled with conventional ablative materials. The open cell configuration makes it easier for the ablative material to flow and become infused into the mold. In addition, the use of a lattice as the reinforcing phase of the ablative material, enhances its shear strength and makes it more resistant to aerodynamic spalling. Furthermore, the three-dimensional lattice structures make the lattice-reinforced composite more designable compared with traditional two-dimensional structures. However, the mechanism of lattice enhancement in addition to the main control parameters is still unclear and corresponding research works are imperative.

Current research on these types of problems has mostly been performed experimentally with lattice webs to reinforce the foam structures [13–16]. Yan et al. [13] proposed to reinforce polyurethane foam with lattice webs made of glass fibers. They found that the lattice webs could significantly improve the load-bearing capacity and energy-absorbing properties of the structure under quasi-static axial loading. In contrast to Yan's approach, Shi et al. [14] used continuous trapezoidal lattice webs as the reinforcing phase for closed-cell polyvinyl chloride (PVC) foam. They found that, by performing compression experiments, the lattice webs changed the damage modes of the foam. Tao et al. [15]

---

reinforced rigid polyurethane foam with a lattice and found that the lattice had a significant effect on the stress dissipation and fracture form of the structure. Both compression and bending performance tests were used in that study. Zhao et al. [16] fabricated conical lattice stitched foam sandwich structures by weaving, and found that the shear and flexural strengths of the hybrid structure were almost twice that of the foam sandwich structure. All researches at present are still limited to lattice webs, and there is less research on lattice reinforced soft material.

Theoretical models for these issues include root-reinforced soil models and composite interface failure mechanisms. The theoretical basis of the mechanical model of root-reinforced soil is the Mohr-Coulomb strength theory. Wu et al. [17–20] obtained the shear-reinforced strength of soil by using orthogonal and oblique roots through mechanical analysis. Pollen et al. [21,22] suggested that the external loads were carried by parallel root bundles and once a root break occurs, then the loads were redistributed among the remaining roots. Schwarz [23] did further optimize the fiber bundle model to obtain the root bundle enhancement model. Fan [24] considered the increment of shear strength of the soil as the sum of the enhancement capacity of the roots for various deformation modes. Ekanayake [25,26] suggested that the energy consumed by the root-soil composite under load, was proportional to the shear strength. Furthermore, Zhou et al. [27,28] derived the incremental shear strength of the composite by analyzing the contribution of various energies to its fracture toughness. However, all the above models consider the root system as a flexible material, and only consider the effect of the tensile of the root system on shear.

The theoretical study of interfacial failure of composites started with the work by Cox et al. [29–31] They concluded that the shear stress at the interface is largest at the end of the fiber and least in the middle. Kelly and Tyson [32] argued that the shear stress at the interface was uniformly distributed. Hiller Borg et al. [33] proposed an elastic softening cohesion model. The model assumed that the shear stress at the interface first increased linearly, and then decreased as the interface displacement increased. When the damage became accumulated to a certain level, the interface became debonded. In contrast to the bilinear model, Zhao [34] argued that the interface entered the yield state after the elastic state, and debonded when the yield region disappeared completely.

Based on the root-reinforced soil principle of trees, this study has presented a matrix combined with a three-dimensional lattice to build a lattice-reinforced composite (LRC). Firstly, this study reported on the fabrication of three composites with different configurations (pyramidal, tetrahedral, and Kagome) of the lattice as the reinforcing phase. Their shear strength under in-plane shear loading was measured experimentally. Then, an analytical formula was derived for the effective shear strength of the LRC under in-plane shear loading. Finally, the effect of topological parameters on the shear strength of the LRC, was investigated.

## 2. Experimental study

### 2.1. Materials and manufacture

The schematic diagram of the LRC is shown in Fig. 1. The LRC of three configurations (pyramidal, tetrahedral, and Kagome) were
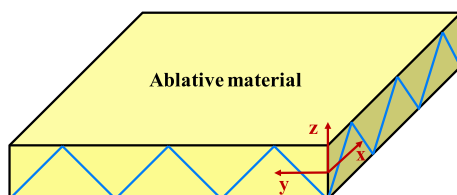


**Fig. 1.** Schematic of the LRC.

prepared, and their shear response was investigated at different relative densities (5 %, 8 %, and 11.5 %). The fabricated LRC specimen, with a relative density of 11.5 %, is shown in Fig. 2. Comparative experiments with the lattice specimen and the matrix specimen, were also examined. The LRC was manufactured by using additive manufacturing. All specimens were printed with the Stratasys objet30 pro printer. The failure mechanism of 3D printing has been studied by scholars [35–38], and this paper focused on shear failure of the LRC. The specific material parameters are shown in Table 1. The material used for printing the lattice was Vero White Plus (RGD835). The material used for printing the matrix was SUP706, which is a quite brittle material. As shown in Table 2, the rod length $l_0$, single core length $L$, rod width $t$, and angle between the rods and the bottom surface $\omega$, were the key parameters describing the LRC. The lengths of the nodes were $b = 0.5\,t$ and $c = \sqrt{2}t/2$, and the width of the nodes was $t_0 = \sqrt{2}t/4$. For the LRC of the three configurations, $l_0$ was 4.2 mm and $\omega$ was 45°. Table 2 also presents the dimensionless relative densities of the lattice for the three different configurations. The dimensionless parameters are $\bar{L} = (l_0\cos\omega + t)/t$ and $\bar{l} = l_0/t$. The thicknesses of the rods at three relative densities for the three configurations of the lattice are listed in Table 3.

The shear response of the LRC is dependent on the shear direction. Hence, the effect of shear direction on shear strength has also been investigated in the present study. The definition of shear direction is shown in Fig. 3. For the lattice shown in Fig. 3a, the shear direction was determined by the angle $\alpha$. The shear direction $\alpha$ of the applied shear stresses $s_{13}$ and $s_{23}$ in Fig. 3b were 0° and 90°, respectively. Unless otherwise specified, all measurements in this study were performed at $\alpha = 0°$.

### 2.2. Experimental method

The shear strength of the LRC was measured according to the in-plane shear test standard for composite materials: ASTM D7078M-05 [39] (Standard test method for shear properties of composite materials
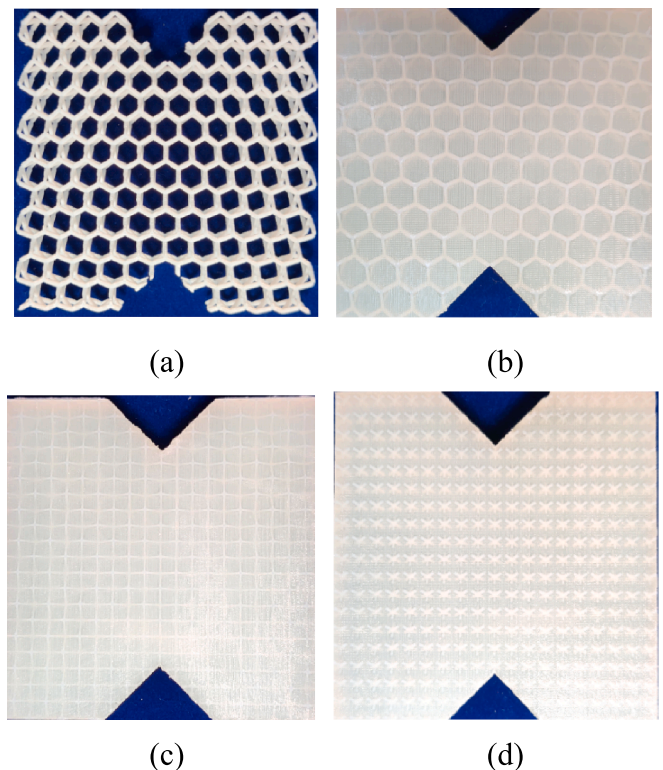


**Fig. 2.** The fabricated specimen: (a) the unfilled Tetrahedral configuration, (b) the Tetrahedral LRC, (c) the Pyramidal LRC, (d) the Kagome LRC.

**Table 1**
Mechanical properties of materials used for printing the lattice and matrix.

| Parameters | Relative density $\rho$ (g/cm$^3$) | Young modulus E (MPa) | Yield strength $\sigma$ (MPa) |
|---|---|---|---|
| RGD835 | 1.175 | 1574 | 74 |
| SUP706 | 1.096 | 0.36 | 0.12 |

by V-notched rail shear method)) (see Fig. 4). In order to reduce the influence of size effect, the LRC of three configurations had at least 7 lattices in the shear direction. All experiments were conducted on a universal testing machine (SUST CMT5205) with a nominal displacement rate of 1 mm / min. The failure process was captured by a CCD camera, with a sampling frequency of 60 Hz and a resolution of 1600 × 1200 pixels.

### 2.3. Experimental results

The damage process of the tetrahedral LRC with a relative density of 11.5 % under shear loading is shown in Fig. 5. The LRC was initially in an elastic state under in-plane shear loading, followed by a gradual cracking of the matrix. The cracks became finally too large, the lattice slipped or became fractured, and the LRC was finally damaged.

Fig. 6 presents the shear strengths of the LRC with three lattice configurations under in-plane shear loading. The experimental results show that the shear strength of the LRC with three lattice configurations did gradually increase with an increasing relative density. For a constant relative density, the shear strength of the LRC with the Kagome configuration was the largest, followed by the tetrahedral and pyramidal configurations.

Typical stress–strain curves for the tetrahedral LRC with a relative

density of 11.5 %, are shown in Fig. 7. Also, the stress–strain relationship for the lattice alone, and for the matrix alone, has been compared under in-plane shear loading (see Fig. 7). It is clear from Fig. 7 that the shear strength increment has resulted in a significantly higher force level in the in-plane shear for the tetrahedral LRC, as compared with the combined effect of just the matrix alone and the lattice alone. This would be referred to as the interaction effect. The shaded area in Fig. 7 represents the incremental shear strength caused by the interaction effect. This latter type of effect can also be represented by the images on the right side of Fig. 7, and certainly by Eq. (1).

$$\tau_{\text{composite}} > \tau_{\text{lattice}} + \tau_{\text{matrix}} \tag{1}$$

where $\tau_{\text{composite}}$ is the shear strength of the LRC, $\tau_{\text{lattice}}$ denotes the shear strength of the lattice, and $\tau_{\text{matrix}}$ indicates the shear strength of the matrix.
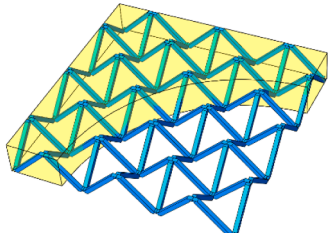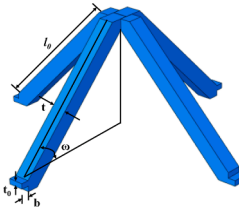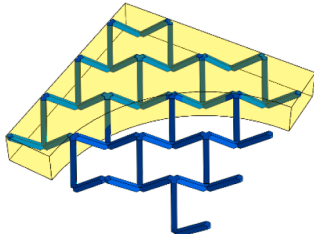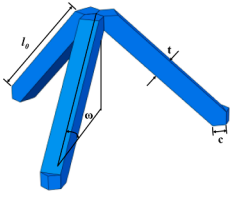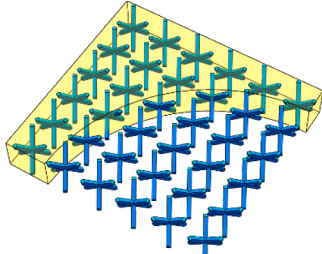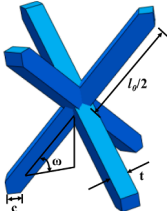
## 3. Theoretical modeling

To study the mechanism of interaction and the influencing factors, a theoretical model was developed.

**Table 3**
The width, $t$, of the rod of three configurations of the LRC.

| Parameters | Pyramidal LRC | Tetrahedral LRC | Kagome LRC |
|---|---|---|---|
| $\rho = 5\%$ | 0.56 | 0.53 | 0.37 |
| $\rho = 8\%$ | 0.7 | 0.66 | 0.47 |
| $\rho = 11.5\%$ | 0.85 | 0.79 | 0.59 |

**Table 2**
Schematics of the LRC with three types of truss core configurations.

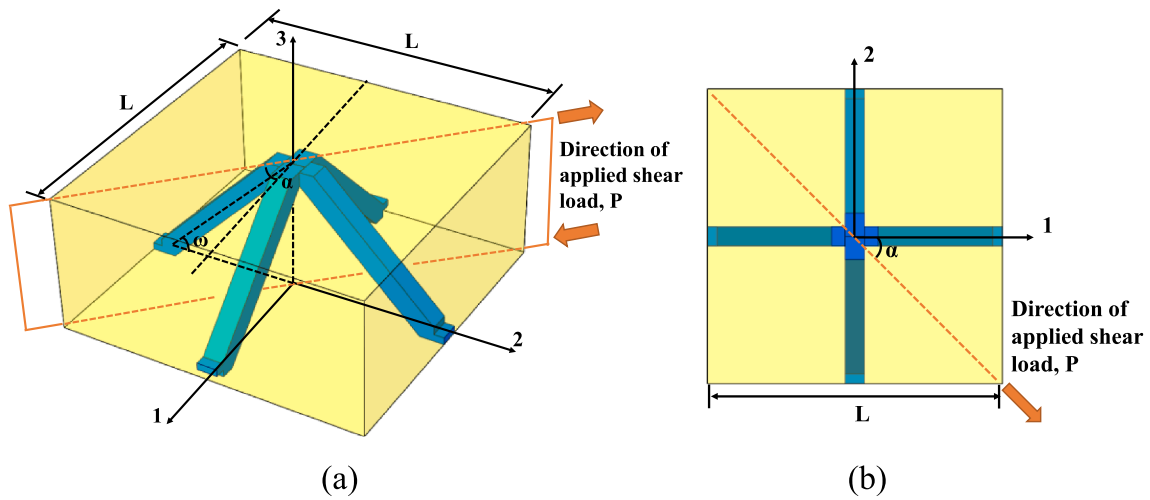| The LRC | Truss core | Relative Density |
|---|---|---|
| *Pyramidal configuration* |  | $\overline{\rho} \approx \dfrac{2}{\overline{l}^2 \sin\omega(\cos 2\omega + 1)}$ |
| *Tetrahedral configuration* |  | $\overline{\rho} \approx \dfrac{4}{\sqrt{3}\overline{l}^2 \sin\omega(\cos 2\omega + 1)}$ |
| *Kagome configuration* |  | $\overline{\rho} \approx \dfrac{3}{\overline{l}^2 \sin\omega}$ |

**Fig. 3.** Schematic of shear direction: (a) schematic diagram showing a single core with shear direction, and (b) top view of a single core.
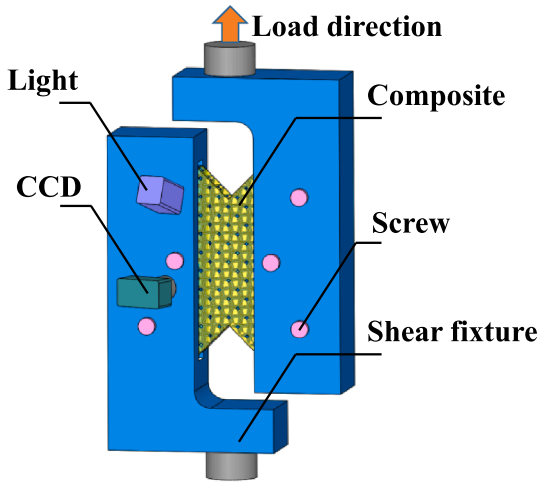


**Fig. 4.** Measurement of the in-plane shear strength of the LRC.

### 3.1. Shear response of the LRC

The shear strength of the LRC has here been assumed to be the sum of the shear strength of the matrix, shear strength of the lattice enhanced phase, and shear strength due to the interaction effect. It can be expressed by Eqs. (2) and (3).

$$\tau_{composite} = \Delta\tau + \tau_{matrix} \tag{2}$$

$$\Delta\tau = \tau_l + \tau_i \tag{3}$$

where $\Delta\tau$ represents the total shear strength increment caused by the addition of the lattice reinforcement phase. Furthermore, $\tau_{composite}$, $\tau_{matrix}$, $\tau_l$ and $\tau_i$ are the in-plane shear strength of the composite, matrix, lattice reinforcing phase, and interaction effect, respectively.

The essence of the lattice enhancement mechanism of the matrix was that the presence of the lattice made the matrix more resistant to cracking. Compared with the matrix, the LRC can absorb more energy for shear damage to occur. The strengthening effect of the lattice as the reinforcing phase to the matrix was mainly reflected in three aspects: (i) the lattice could prevent the generation and expansion of microcracks in
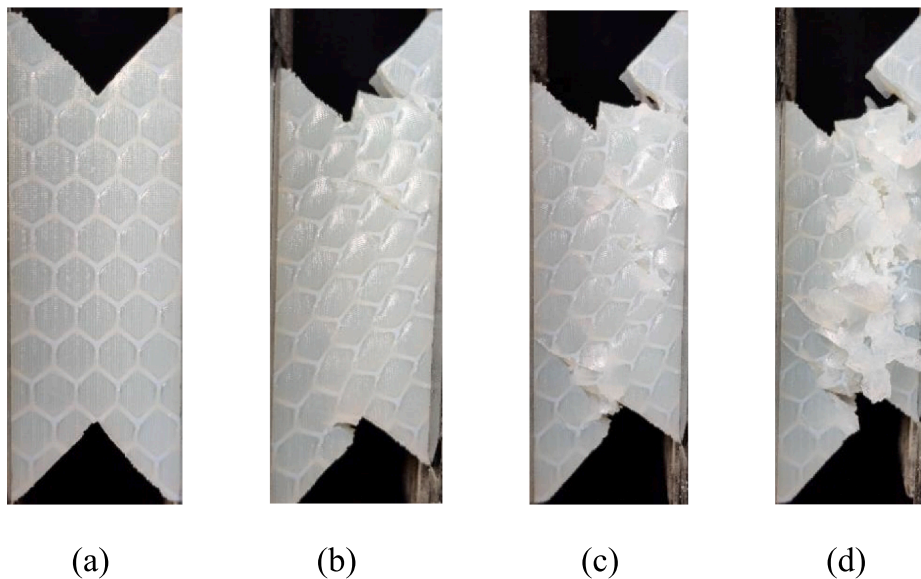


**Fig. 5.** Shear damage process of tetrahedral LRC: (a) tetrahedral LRC was in elastic stage; (b) cracks appeared first in the matrix at the structural weakness; (c) the shear load gradually increased and the damage occurred in the lattice; (d) the cracks through the structure and the tetrahedral LRC was completely damaged.
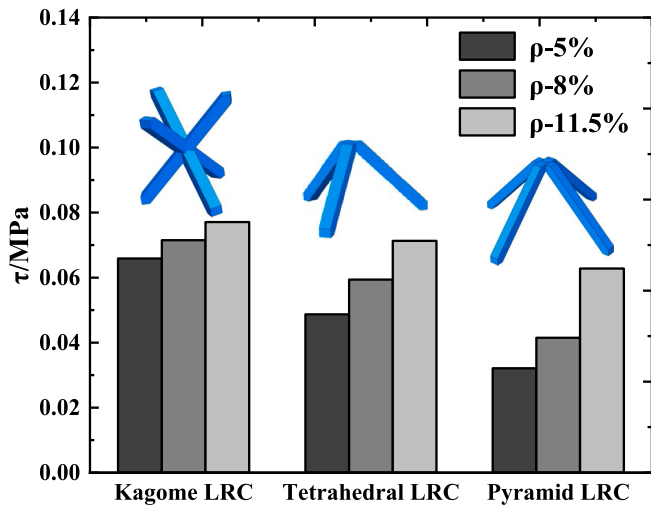
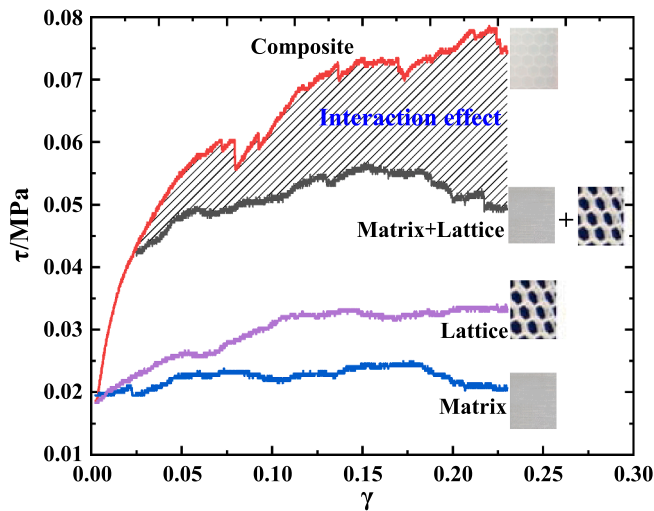**Fig. 6.** Strength of LRC of three configurations under shear load.



**Fig.7.** The interaction effect of the LRC.

during the deformation of the matrix, a tangential force parallel to the interface was generated between the lattice-reinforced phase and the matrix. In order to achieve the coordination of the deformation, a constraint was created by the deformation of the lattice-enhancement phase, and this constraint produced an additional pressure acting on the matrix. Conversely, the matrix applied a tensile force on the lattice-reinforced phase. This is illustrated in Fig. 8.

The force analysis of the LRC is shown in Fig. 9. The rod AB was subjected to a tension under the action of an in-plane shear load. When a shear damage occurred in the LRC, the lattice would not produce a tensile damage if the tensile strength of the lattice was large enough to be greater than the interfacial bond strength. It would rather undergo debonding and slipping. On the contrary, the lattice would undergo a tensile damage if the tensile strength of the lattice was smaller than the interfacial bond strength. Under the action of an in-plane shear load, the interaction effect would pass two stages [27,28]. The axial force of the stretched rods and the interfacial bond strength would balance each other, and the lattice would become deboned; As the load further increased, the tensile rods of the lattice would undergo a frictional slip, at which time the interfacial properties were determined by the interfacial friction strength.

The critical force analysis is shown in Fig. 9b. At the surface of the lattice tensile rod, the axial stress and the shear stress at the interface of the lattice and the matrix balance each other, we could get

$$\left(\frac{dT}{dl}\right)dl \cdot t^2 = \tau \cdot 4tdl \tag{4}$$

where $T$ represents the axial force of the tensioned rods, $\tau$ represents the shear stress between the lattice and the matrix, and $t$ represents width of the rod.

The axial stress of the tensioned rod was gradually decreasing from one end to the other, so Eq. (4) could be integrated to obtain Eq. (5).

$$T = \frac{4\tau l}{t} \tag{5}$$

Zhou et al. [27,28] presented the work required for the root system to be presented as Eq. (6).

$$G_d = \frac{\int_0^l T \cdot t^2 dl}{A} \tag{6}$$

where $G_d$ denotes the energy absorbed per unit area when a stretched rod is being deboned, and A denotes the projected area of a single core. The process of damage occurring in the composite is equivalent to the process of destabilization and expansion of the cracks in the composite. Hence, the shear strength of the tetrahedral LRC obtained when the stretched rod is being deboned can be expressed as presented in Eq. (7).

$$\tau_i = \frac{8\tau_d t}{3\sqrt{3}l_0(\cos 2\omega + 1)} \tag{7}$$

where $\tau_i$ represents the shear strength of the tetrahedral lattice induced by the interaction contribution, $\tau_d$ is the interfacial bond strength, and $\tau_d = 0.0572$ MPa as measured experimentally.

the matrix; (ii) the lattice as the reinforcing phase could increase the shear strength of the matrix; (iii) when cracks appeared in the matrix, the rods of the lattice could cross the cracks and bear the load, so that the LRC had a certain ductility.

When subjected to external loads, the matrix, and the lattice in the LRC were deformed in a coordinated manner. The elastic modulus of the lattice was much larger than the elastic modulus of the matrix. When the load increased, there was a mutual motion, or movement, of the lattice-reinforced phase and the matrix, and this motion resisted on the interfacial bond strength between the lattice and the matrix. Therefore,
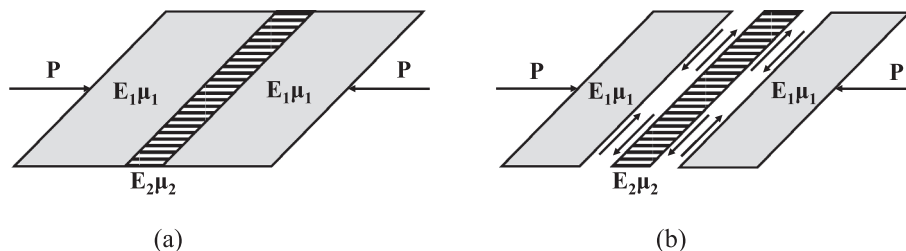


(a)

(b)

**Fig. 8.** Force analysis of the LRC: (a) the matrix and the lattice in the LRC bear the load to coordinate deformation; (b) misalignment between the matrix and the lattice due to difference in elastic modulus.
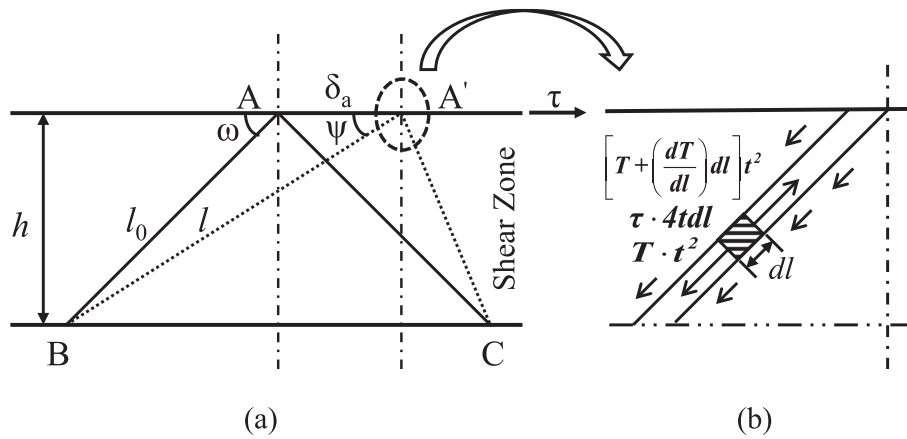
**Fig. 9.** Schematic of the critical state force analysis of LRC debonding: (a) deformation analysis of a lattice tensile rod; (b) debonding occurs when the shear stress on the surface of the tensioned rod reaches the interfacial bond strength.

### 3.2. Validation of the theoretical model

As presented in Fig. 10, the predicted values of the theoretical model were compared with the experimental results for a relative density, ρ, of 11.5 %. The theoretical predictions and experimental results of the tetrahedral LRC were found to match well with the discrepancies of 10.3 %, 12.6 %, and 8 %, respectively. Fig. 10 demonstrates the contribution of the mutually induced shear strength increments to the shear strength of the LRC, indicating that it could not be neglected. The three components of the shear strength of the LRC under in-plane shear loading, where the shear strength of the lattice itself (i.e., dominating contribution to the shear strength of the LRC), followed by the shear strength of the matrix itself, and then the shear strength induced by the interactions. There was also a significant increase in shear strength of the tetrahedral LRC compared to the specimen with a matrix only.

### 3.3. Mechanisms of the interaction effects

Based on the analytical results of Eq. (7), the variational pattern of the dimensionless shear strength versus relative density consisted of three components, the LRC, the specimen with a tetrahedral lattice only, and the interaction effect between the tetrahedral lattice and the matrix. The specific analysis results are presented in Fig. 11. For a constant relative density, the dimensionless shear strength of the LRC was the largest, followed by the specimen with a tetrahedral lattice only, and
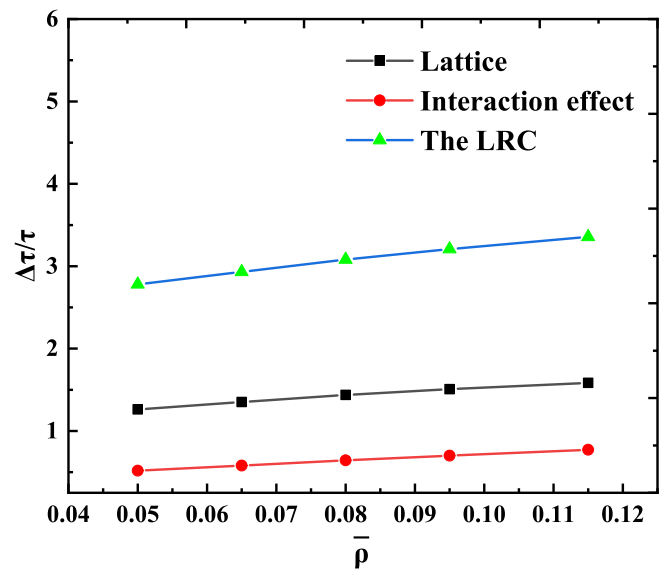


**Fig. 11.** Variational patterns of the individual components of shear strength with relative density.

then the interaction effect between the lattice and the matrix. This showed that after adding the lattice as the reinforcing phase of the matrix, the shear enhancement effect of the lattice itself still played a key role, but the interaction between the lattice and the matrix could not be ignored and had to be considered. When the relative density of the lattice increased, the interaction effect was gradually increased. This has demonstrated that the enhancement effect of the LRC and the enhancement effect of the lattice were similar in magnitude. The interaction effect did also gradually increase, but the magnitude of the enhancement was not as large as that of the lattice.

### 3.4. Effect of the relative density

The variational pattern of the dimensionless shear strength versus relative density of LRCs with pyramidal, tetrahedral and Kagome configurations, is presented in Fig. 12. When the relative density increased, the dimensionless shear strength of the LRCs of all three configurations also increased. For a constant value of the relative density, the dimensionless shear strength of the LRCs with a Kagome configuration was the largest one, followed by the LRCs with tetrahedral configuration, and the LRCs with pyramidal configuration showed the lowest dimensionless shear strength. This result can be explained by three configurations of
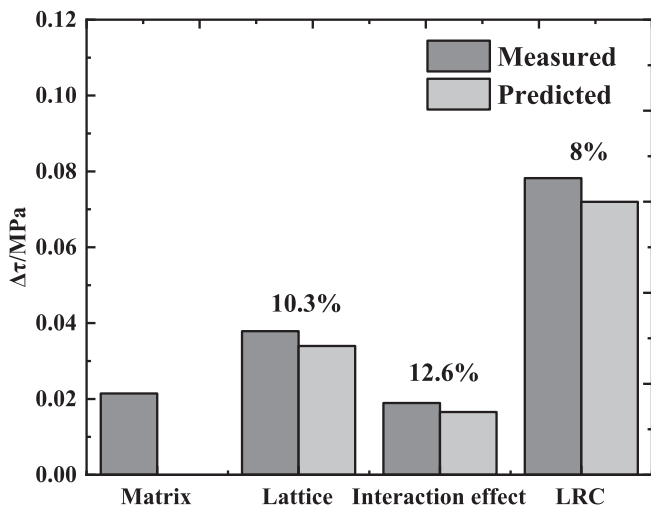


**Fig. 10.** Comparison of experimental and theoretical results for lattice, interaction effect and the tetrahedral LRC.
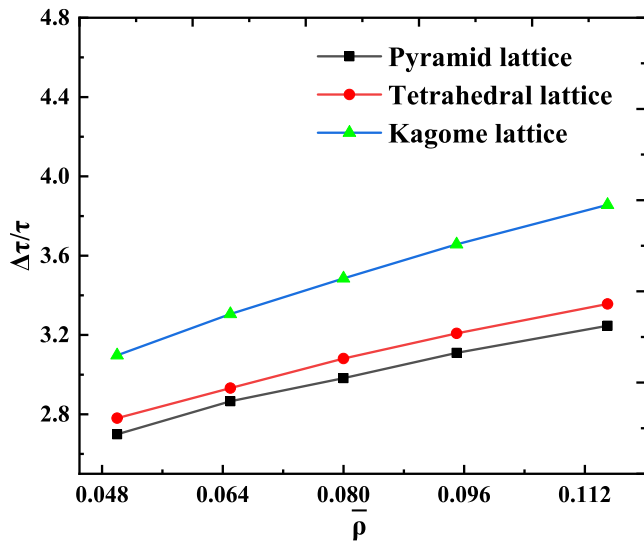
**Fig. 12.** The variation of a dimensionless shear strength versus relative density for three configurations of the LRC.

the LRC dimensionless shear modulus have the same tendency, which was the largest for the Kagome configuration, followed by the tetrahedral configuration, and the smallest for the pyramid configuration. The variational pattern of the shear modulus is represented in Fig. 13. The variational pattern of the composites with an increasing relative density, coincided with the shear modulus.

### 3.5. Effect of the shear angle and the single core size

Analytical predictions have indicated that the shear strength of the pyramid LRC lattice was related to the shear angle, $\alpha$. This was confirmed by the dimensionless shear strength versus relative density (as demonstrated in Fig. 14). For the pyramid LRC lattice, the shear strength of the LRC was larger for a loading angle $\alpha = 45°$.

Finally, the effect of a single core size on the shear strength increment of the LRC, has also been investigated in the present study. The results of this analysis are shown in Fig. 15. For a constant relative density, the effect of the LRC shear enhancement for the three configurations did first decrease sharply when the size of the cores increased,
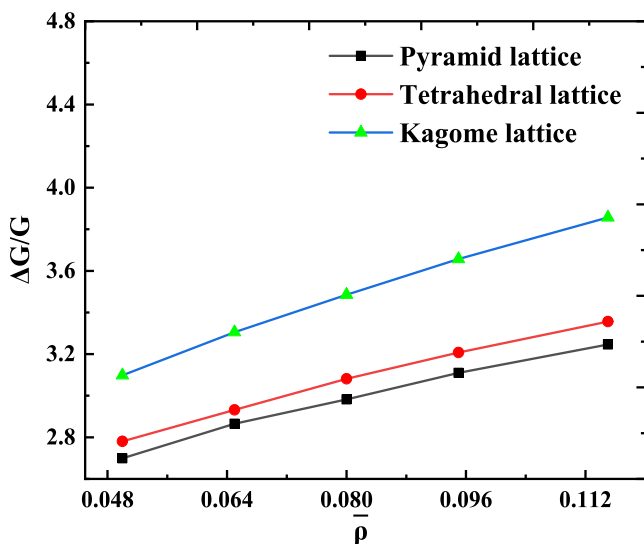


**Fig. 13.** The variation of a dimensionless shear modulus versus relative density for three configurations the LRC.
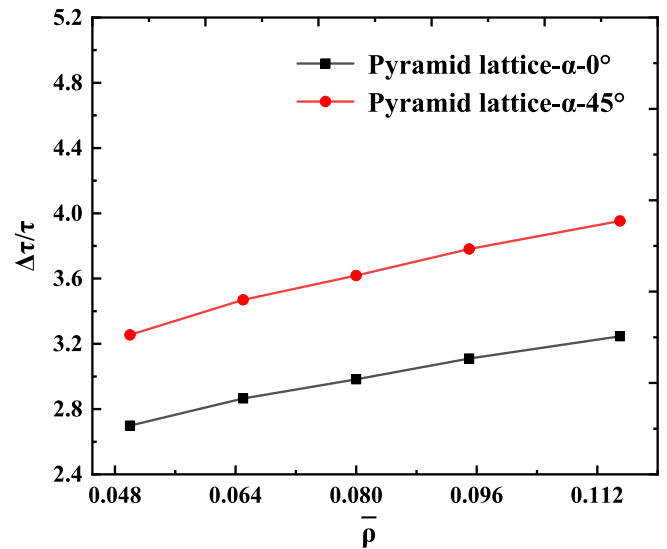


**Fig. 14.** Variation of dimensionless shear strength, $\Delta\tau/\tau$, versus relative density,$\bar{\rho}$, for pyramidal LRC and two different loading angles, $\alpha$.
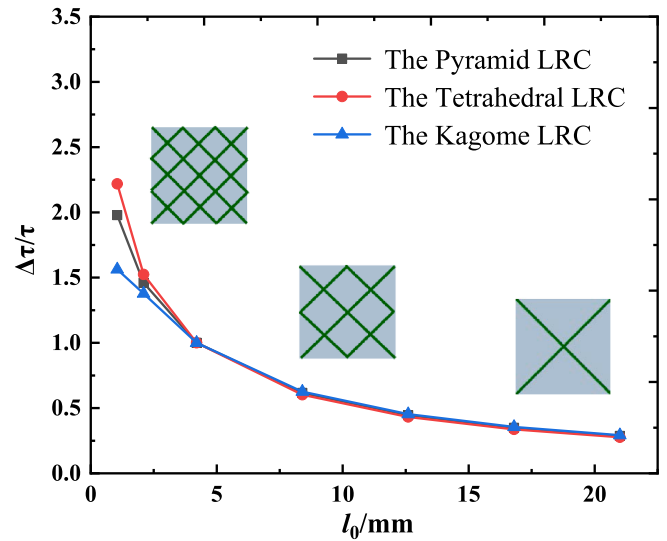


**Fig. 15.** Effect of single core size, $l_0$, on the increment of shear strength, $\Delta\tau/\tau$.

and then leveled off gradually. Even though the size of the core continued to increase, the effect on the LRC shear enhancement was small. This indicated that we could design smaller lattices at the outer end of the heat-resistant bottom when the effect of LRC shear enhancement was significant and could better resist the high-speed airflow.

### 4. Conclusions

The three-dimensional lattice reinforced matrix structure was a newly developed hybrid structure with high performance and light weight. The in-plane shear behavior of this mixed composite structure has been investigated by using a combined experimental and theoretical approach. Results indicated that the combination of a three-dimensional lattice and a matrix could significantly improve the shear strength of the composite structure, which was greater than the sum of the contributions of lattice and matrix structures. The variational patterns of the LRCs, with pyramidal, tetrahedral, and Kagome configurations under in-plane shear loading, were investigated. The increase in shear strength was primarily due to the interaction effect between the rods of the lattice

and the matrix. The main source of the interaction was the stretching debonding in the interface between the lattice rod and the matrix. The interaction effect did gradually become enhanced as the relative density increased. In addition, the effect of lattice configuration on the shear strength was also obtained, with the most significant increase in shear strength for the LRC with a Kagome configuration.

## CRediT authorship contribution statement

**Peixin Yang:** Conceptualization, Methodology, Writing – original draft. **Wu Yuan:** Writing – review & editing, Funding acquisition. **Hongwei Song:** Data curation. **Chenguang Huang:** Supervision.

## Declaration of Competing Interest

The authors declare that they have no known competing financial interests or personal relationships that could have appeared to influence the work reported in this paper.

## Data availability

Data will be made available on request.

## Acknowledgments

## References

[1] Winter M W, MCDANIEL R D, CHEN Y-K, et al. Radiation Modeling for Reentry of Hayabusa Sample Return Capsule [J]. Journal of Spacecraft and Rockets, 2019, 56 (4).

[2] Albano M, Nenarokomov AV, Pastore R, et al. Thermo-mechanical characterization of carbon-based ceramic foams for high temperature space application [J]. High Temp-High Pressures 2022;51(2):89–108.

[3] Delfini A, Pastore R, Santoni F, et al. Thermal analysis of advanced plate structures based on ceramic coating on carbon/carbon substrates for aerospace Re-Entry Re-Useable systems [J]. Acta Astronaut 2021;183:153–61.

[4] Pastore R, Delfini A, Santoni F, et al. Space Environment Exposure Effects on Ceramic Coating for Thermal Protection Systems [J]. J Spacecraft Rockets 2021;58 (5):1387–93.

[5] Cheng H, Hong C, Zhang X. An overview on low-density ablators [J]. J Harbin Instit Technol 2018;50(5):1–11.

[6] Yang C, Dong Y. Progress and Requirements of Thermal Protection Materials for Deep Space Exploration in China [J]. Aerospace Mater Technol 2021;51(5):26–33.

[7] Deng H, Tan J, Tan Z, et al. The Low Density Materials Reinforced by Honeycomb for Long Time Ablation and Thermal Protection [J]. Aerospace Mater Technol 2014;44(1):89–91.

[8] Wang C, Liang X, Sun B, et al. Application of Low Density Ablative Material on Shenzhou Spacecraft [J]. Aerospace Mater Technolgy 2011;41(2):5–8.

[9] Ashby MF. The properties of foams and lattice [J]. Philos Trans Roy Soc 2006;364: 15–30.

[10] Habib FN, Iovenitti P, Masood SH, et al. Fabrication of polymeric lattice structures for optimum energy absorption using Multi Jet Fusion technology [J]. Mater Des 2018;155:86–98.

[11] Mahmoud D, Elbestawi MA. Selective laser melting of porosity graded lattice structures for bone implants [J]. Int J Adv Manuf Technol 2019;100(9).

[12] Moongkhamklang P, Deshpande VS, Wadley H. The compressive and shear response of titanium matrix composite lattice structures [J]. Acta Mater 2010;58 (8):2822–35.

[13] Fan Z, Fang H, Zhuang Y, et al. Experimental study on energy absorption of the foam sandwich composite enhanced lattice web under quasi-static compression [J]. Fiber Reinforced Plastics/Compos 2017;1:10.

[14] Shi C, Wang J, Zhu J, et al. Flatwise compression properties of trapezoidal lattice-web reinforced foam core sandwich composites [J]. Acta Materiae Compositae Sinica 2022;39(2):600.

[15] Tao Y, Li P, Zhang H, et al. Compression and flexural properties of rigid polyurethane foam composites reinforced with 3D-printed polylactic acid lattice structures [J]. Compos Struct 2022;279.

[16] Zhao Y, Yan S, Jia J. Fabrication and Statics Performance of Pyramidal Lattice Stitched Foam Sandwich Composites [J]. CMES-Comput Model Eng Sci 2021;126 (3):1274.

[17] Gray DH, Al-Refeai T. Behavior of Fabric-Versus Fiber-Reinforced Sand [J]. J Geotech Eng 1986;112(8):181–7.

[18] Gray DH, Ohashi H. Mechanics of Fiber Reinforcement in Sand [J]. J Geotech Eng 1983;109(3):335–53.

[19] Shewbridge SE, Sitar N. Deformation Characteristics of Reinforced Sand in Direct Shear [J]. J of Geotech Engrg 1989;115(8):1134–47.

[20] Wu TH, McKinnell WP, Swanston DN. Strength of tree roots and landslides on Prince-of-Wales-Island, Alaska [J]. Can Geotech J 1979;16(1):19–33.

[21] Pollen N, Simon A. Estimating the mechanical effects of riparian vegetation on stream bank stability using a fiber bundle model [J]. Water Resour Res 2005;41(7).

[22] Schwarz M, Cohen D, Or D. Root-soil mechanical interactions during pullout and failure of root bundles [J]. J Geophys Res 2010;115(F4).

[23] Schwarz M, Lehmann P, Or D. Quantifying lateral root reinforcement in steep slopes - from a bundle of roots to tree stands [J]. Earth Surf Proc Land 2010;35(3): 354–67.

[24] Fan C-C. A displacement-based model for estimating the shear resistance of root-permeated soils [J]. Plant and Soil, 2012, 355(1-2): 103-19.

[25] Ekanayake JC, Phillips CJ. A method for stability analysis of vegetated hillslopes: an energy approach [J]. Can Geotech J 1999;36(6):1172–84.

[26] Ekanayake JC, Phillips CJ. Slope stability thresholds for vegetated hillslopes: a composite model [J]. Can Geotech J 2002;39(4):849–62.

[27] Sui Z, Yi W. A root-reinforced soil mechanics model based on the Griffith fracture criterion [J]. J Central South Univ Forestry Technol 2021;41(6):167–74.

[28] Yunyan Z, Jianping C, Xiaomei W. Research on Resistance Cracking and Enhancement Mechanism of Plant Root in Slope Protection by Vegetation [J]. J Wuhan Univ Nat Sci Ed 2009;55(5):613–8.

[29] Ang KK, Ahmed KS. An improved shear-lag model for carbon nanotube reinforced polymer composites [J]. Compos Part B-Eng 2013;50:7–14.

[30] Cox HL. The elasticity and strength of paper and other fibrous materials [J]. Br J Appl Phys 1952.

[31] Nairn JA. On the use of shear-lag methods for analysis of stress transfer unidirectional composites [J]. Mech Mater 1997;26(2):63–80.

[32] Kelly A, Tyson WR. Tensile properties of fibre-reinforced metals: Copper/tungsten and copper/molybdenum [J]. J Mech Phys Solids 1965;13(6):329–38.

[33] Hillerborg A, Modéer M, Petersson P-E. Analysis of crack formation and crack growth in concrete by means of fracture mechanics and finite elements. Cem Concr Res 1976.

[34] Zhao Y, Yuan H, Han J. Analysis of the macroscopic interfacial behaviour of the fibre pullout using elastic-plastic cohesive model. Chin J Theor Appl Mech 2015;47 (1):127–34.

[35] Gao X, Qi S, Kuang X, et al. Fused filament fabrication of polymer materials: A review of interlayer bond [J]. Addit Manuf 2021;37.

[36] Mazzei Capote GA, Rudolph NM, Osswald PV, et al. Failure surface development for ABS fused filament fabrication parts [J]. Additive Manuf 2019; 28: 169–175.

[37] Osswald PV, Obst P, Capote GAM, et al. Failure criterion for PA 12 multi-jet fusion additive manufactured parts [J]. Addit Manuf 2021;37.

[38] Rankouhi B, Javadpour S, Delfanian F, et al. Failure Analysis and Mechanical Characterization of 3D Printed ABS With Respect to Layer Thickness and Orientation [J]. J Fail Anal Prev 2016;16(3):467–81.

[39] Standard test method for shear properties of composite materials by V-notched rail shear method [J]. 2005.